

XMM-Newton observations of Abell 2255 : a test case of a merger after ‘core-crossing’.

Irini Sakelliou^{1,2}, Trevor J. Ponman¹,

¹*School of Physics & Astronomy, University of Birmingham, Edgbaston, Birmingham B15 2TT*

²*Max-Planck-Institute für Astronomie, Königstuhl, 17, D-69117, Heidelberg, Germany*

5 July 2018

ABSTRACT

It has been known that Abell 2255 is not a relaxed cluster, but it is undergoing a merger. Here, we report on the analysis of the XMM-Newton observations of this cluster. The X-ray data give us the opportunity to reveal the complexity of the cluster, especially its temperature distribution. The integrated spectrum is well fitted by a single temperature thermal model, indicating a mean temperature of ~ 7 keV. However, the cluster is not isothermal at this temperature: its eastern regions are significantly cooler, at ~ 5.5 keV, whilst towards the West the temperature reaches ~ 8.5 keV.

These temperature asymmetries can be explained if Abell 2255 has been assembled recently by the merging of smaller subunits. It is now in the phase after the cores of these subunits have collided (the ‘core-crossing’ phase) some 0.1-0.2 Gyr ago. A comparison with numerical simulations suggests that it will settle down into a single relaxed cluster in $\sim (2-3)$ Gyr.

Key words: X-rays : galaxies : clusters – intergalactic medium – galaxies : clusters : individual (Abell 2255)

1 INTRODUCTION

After the first X-ray observations, it became apparent that Abell 2255 is a cluster that is currently under formation, growing by the accumulation of smaller subunits. The ROSAT images showed that the cluster is elongated along the East-West direction, and that the centroid of the X-ray emission does not coincide with any large cluster galaxy (Burns et al. 1995, Feretti et al. 1997). The spectral analysis of Davis & White (1998) found significant temperature structure in its intracluster medium (ICM), which they also attributed to a recent merger event. Abell 2255 was observed by Chandra with the ACIS-I detector for a total of 39 ksec. The Chandra data set, was used by Davis, Miller, & Mushotzky (2003), to investigate the X-ray properties of the cluster galaxies. It has also been observed by XMM-Newton and Fig. 1(a) shows the XMM-Newton mosaic. In Fig 1(b) we present an overlay of the X-ray contours onto an optical image of the central regions of Abell 2255. The X-ray contours are obtained from the XMM-Newton observations that will be presented in the subsequent sections of this paper.

Optically, as can be seen in Fig. 1(b), a very intriguing property of Abell 2255 is that the brightest galaxies are arranged in a chain, whose orientation coincides with the major axis of the elliptical X-ray emission. The cluster has an unusually high velocity dispersion of ~ 1200 km s⁻¹, and

the two brightest galaxies [galaxies A and B in Fig. 1(b)] are separated by ~ 2600 km s⁻¹ (Burns et al. 1995). Performing deep multicolour photometry in a large field around the cluster, Yuan, Zhou, & Jjang (2003) showed that at radii $> (10-15)$ arcmin there are small groups of galaxies, that appear to rotate around the central core of Abell 2255.

In the radio Abell 2255 contains a central radio halo (see, for example, Giovannini, Tordi & Feretti 1999, and references there-in), and a number of tailed radio galaxies. More recently, Govoni et al. (2005) presented a high sensitivity radio image of Abell 2255 which reveals the detailed structure of its radio halo and a possible radio relic. Radio halos are rare radio sources, and they have been found in the inner, 1 Mpc of X-ray bright and hot clusters [see Giovannini & Feretti (2000) for some recent examples]. They locate the site of relativistic electrons and magnetic fields in clusters. The presence of such a halo in Coma, in conjunction with its X-ray morphology, motivated the suggestion by Burns et al. (1994) that radio halos are fuelled by cluster collisions, and are associated with clusters undergoing disturbances from recent or on-going merging events. Since the first discoveries, significant advances have been made in understanding their origin (e.g. Buote 2001).

Thus, the X-ray, optical and radio data provide evidence that Abell 2255 is currently active, and other surrounding structures might be interacting with it. This impression is

arXiv:astro-ph/0601382v1 18 Jan 2006

Table 1. Pointing Information

(I) Rev	(II) Obs	(III) α (2000)	(IV) δ (2000)	(V) Instr.	(VI) <i>Exp</i> ksec	(VII) <i>Exp_{corr}</i> ksec
525	0112260501	17 12 59.920	+64 03 25.00	MOS1	8.558	4.307
				MOS2	8.645	4.466
				PN	4.326	1.665
548	0112260801	17 12 58.460	+64 04 49.20	MOS1	16.468	10.810
				MOS2	16.504	10.657
				PN	11.918	4.068

NOTES : (I)-revolution number; (II)-observation number; (III)-pointing *RightAscension*; (IV)-pointing *Declination*; (V) EPIC Instrument; (VI) Exposure time (live time for the central CCD); (VII) Reduced Exposure time, after the subtraction of the bright background flares (see text for more details).

not very surprising if one thinks that Abell 2255 is a member of the rich North Ecliptic Pole supercluster, that contains at least 21 galaxy clusters, as was revealed by the analysis of the *ROSAT* All-Sky Survey data by Mullis et al. (2001).

We have observed Abell 2255 with *XMM-Newton* in order to uncover its dynamical state, decide on its past history and future evolution, and derive vital information that would help us to test the results of the numerical simulations of merging clusters. In this paper, we present the analysis and results of the *XMM-Newton* observations: the observations are described in Section 2; Sections 3 and 4 are devoted to the presentation of the X-ray properties of the cluster, as found from the *XMM-Newton* data analysis; in Section 5 we compare the *XMM-Newton* and *ROSAT* results; finally, in Section 6 we discuss a possible dynamical scenario that can describe well the data.

The redshift of Abell 2255 is $z=0.0806$ (NED), and throughout this paper we use $H_0 = 71 \text{ km s}^{-1} \text{ Mpc}^{-1}$, $\Omega_M=0.3$, and $\Omega_\Lambda=0.7$, giving a scale of $1.499 \text{ kpc}''$. The Galactic hydrogen column for the direction of Abell 2255 is $N_{\text{H,G}} = 2.6 \times 10^{20} \text{ cm}^2$.

2 *XMM-Newton* OBSERVATIONS

Abell 2255 was observed by *XMM-Newton* for a total of ~ 25 ksec. The observation was split into two: the first part was performed on the 22nd October 2002 (revolution=525), while the second one on the 7th December 2002 (revolution=548). Information about these two pointings is gathered in Table 1. During both observations the EPIC instruments were operating in the PrimeFullWindow (for MOS1 and MOS2), and PrimeFullWindowExtended (PN), and the thin filter was used for all imaging detectors.

2.1 Data Reduction

The raw data from the EPIC instruments were processed with SAS v5.4.1. EMCHAIN and EPCHAIN were used to obtain the calibrated event lists for the MOS and PN instruments respectively. During the processing the parameter *withbadpixfind* was switched on, so that bad pixels that had not been recorded in the calibration files were found and subsequently removed. After the initial processing we confirmed that new bad pixels were found. The calibrated events were filtered

for FLAGS, using the *XMM-Newton* FLAGS #XMMEA_EM and #XMMEA_EP for the two MOS and the PN detectors respectively. Restrictions on the PATTERN were also applied: we kept only events with PATTERN<12 for the MOS cameras, and < 4 for the PN. We also cleaned the event lists for periods of high background. This cleaning process reduced the exposure times to those presented in column (VII) of Table 1.

2.2 Background Treatment

Background data were generated from the ‘blank-sky’ event lists (D. Lumb’s background files; Lumb 2002). The coordinate frames of these fields were converted to the corresponding frames for each *XMM-Newton* pointing of the Abell 2255 observations. The background event lists were filtered for PATTERN and FLAG in the same manner as was done for the data. Periods of high background levels that were still present in D.Lumb’s background files, were removed by applying a $3\text{-}\sigma$ cut-off. Subsequently, the background events were scaled to match the background levels of each instrument and observation by scaling the out-of-field events as in Pratt et al. (2002). The scaling factors we found for MOS1, MOS2 are 1.25 and 1.15 respectively for both observations, consistent with previous findings. However, for the PN detector we found scaling factors that are larger than expected (2.2 for the 0112260801 and 3.5 for the 0112260501 observation).

Given the uncertainty of the scaling factors for the PN detector, we used the blank-sky background files only for the purpose of the spatial analysis. The spectral analysis (see Section 4) concentrates on the properties of the inner region of the cluster (<6 arcmin) leaving enough room for the safe use of local background, as will be demonstrated in Section 4. As a test and to support our choice of the background files used for the spectral analysis, we performed the same fitting procedures as the ones presented in Section 4 adopting the blank-sky scaled files as the background spectra. We found that the derived temperatures are systematically higher than the ones derived with the local background files by $\sim(0.5\text{-}1.0)$ keV, but they always show the same trends.

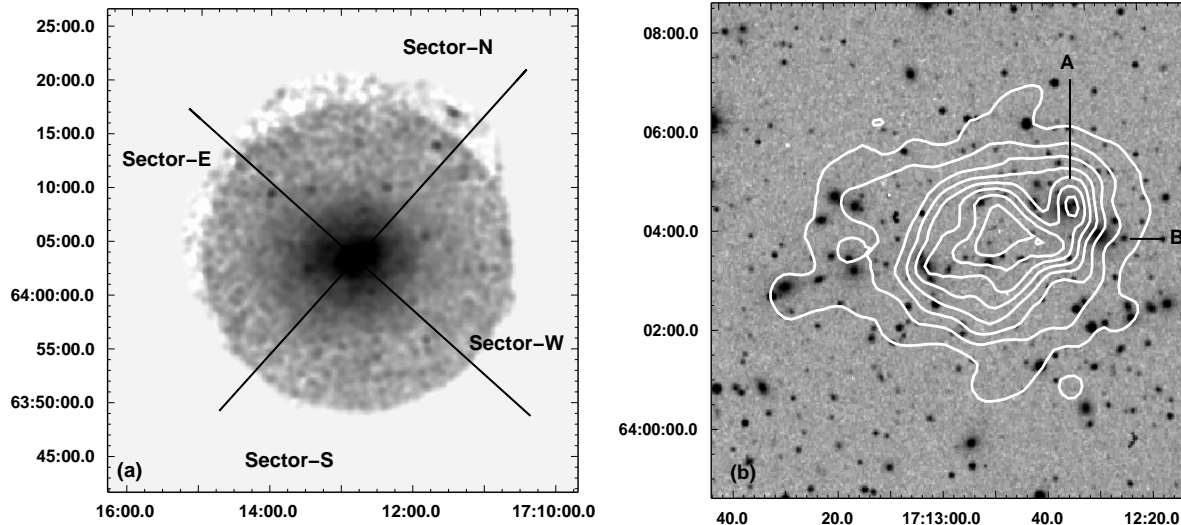


Figure 1. (a) The *XMM-Newton* mosaic of Abell 2255 images from all the instruments and both observations in the (0.5-10.0) keV energy range have been co-added. (b) DSS image of the central region of the cluster overlaid by the X-ray contours of the image shown in (a). The contour levels are linearly spaced from 1.4 to 6.3×10^{-3} $\text{cnt s}^{-1} \text{pix}^{-2}$, where each image pixel is 8 arcsec.

3 SPATIAL ANALYSIS

For the purpose of any subsequent spatial analysis, firstly we created background-subtracted and exposure-corrected images for both observations and each EPIC instrument in the (0.5-10.0) keV energy range. The background and exposure correction was performed as in Sakelliou & Ponman (2004).

The background-subtracted and exposure-corrected images from each camera and observation were added with the SAS task EMOSAIC, after scaling down the PN images to match the efficiency of the MOS detectors. The final mosaic was smoothed with a Gaussian kernel of $\sigma=16$ arcsec. Fig. 1(a) presents this smoothed mosaic. The same figure shows the orientation and boundaries of the four sectors, that were used for the analysis in Sections 3.2 and 4.2.1. In Fig. 1(b) we overlay the X-ray contours onto a DSS image of the central cluster region.

In these images, the cluster appears elongated along the East-West direction, and the most sever disruptions are encountered within the central $\sim(8-10)$ arcmin. As noted before, the peak of the X-ray emission does not appear to coincide with any cluster galaxy.

In the following sections, we demonstrate how the background-subtracted and exposure-corrected images were used to model the over-all light distribution (Section 3.1), and in Section 3.2 to investigate its azimuthal variations.

3.1 2-dimensional analysis

The background-subtracted and exposure-corrected images from each *XMM-Newton* camera were fitted in SHERPA by a 2-dimensional β -model. The fit was restricted to the inner 10 arcmin of the image, and all bright point sources were subtracted. The images from the three *XMM-Newton* cameras were fitted simultaneously. The core radius (r_c), the β -parameter, the location of the x-ray centre, the ellipticity (e), and position angle (θ) were linked and left free, so that

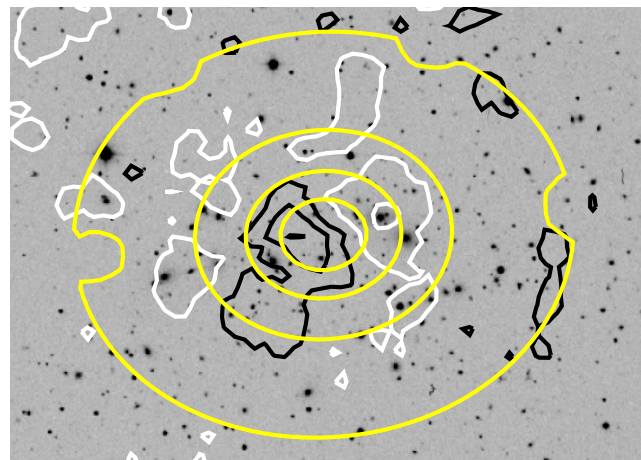


Figure 2. Optical image of the central $\sim(17.3 \times 12.4)$ arcmin² of Abell 2255. The image is overlaid by the contours of the residuals, and the best fitting model derived from the 2-dimensional fit to the X-ray image (see Section 3.1). Positive residuals are shown as white lines, negative as black, and the best fitting model with the grey ellipses.

their values are determined by the fitting procedure. The normalizations of the β -models were free to vary independently for each instrument.

This fitting procedure resulted in the following best fitting parameters: $r_c = 110.8_{-2.3}^{+2.0}$ arcsec = $165.9_{-3.5}^{+3.0}$ kpc, $\beta = 0.37 \pm 0.17$, $e = 0.191 \pm 0.006$, $\theta = 0.048 \pm 0.015$ deg. The X-ray centre is found at $\alpha_{cen} = 17^h 12^m 50^s.38$ $\delta_{cen} = +64^\circ 03' 42''.56$, which does not coincide with any of the big cluster galaxies, as can be also seen in the plot of Fig. 2. The values of the β -index and the r_c derived from this fitting procedure appear lower than their ‘canonical’ values for clusters of galaxies. If we fix the β -index at 0.65, the

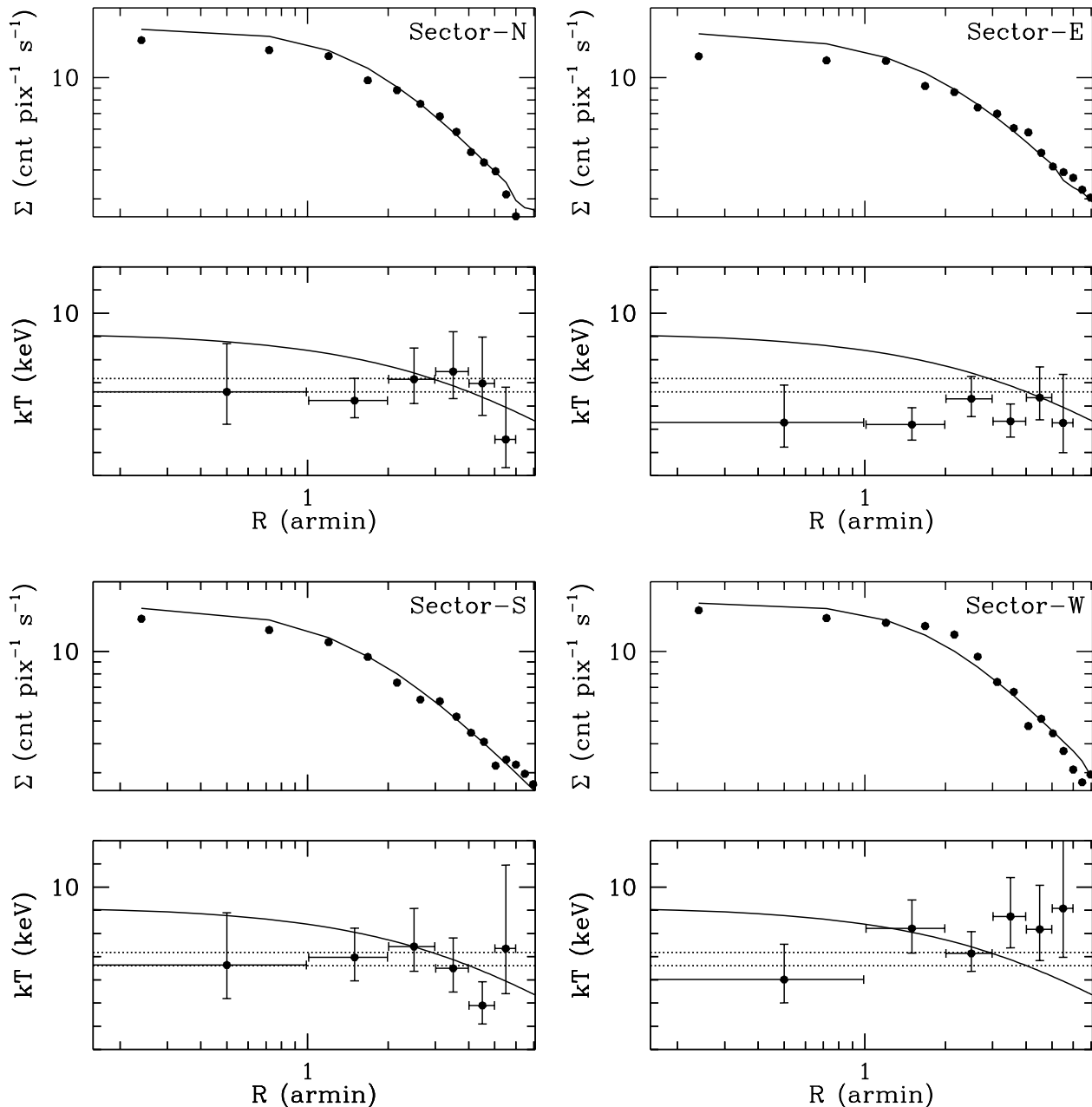


Figure 3. Surface brightness (Σ) and temperature (kT) profiles for each of the four sectors in Abell 2255 shown in Fig. 1(a). The surface brightness as registered on the MOS1 detector only are shown, but the profiles from the other cameras are similar. The solid lines in the surface brightness plots represent the best-fitting model for each sector, found by the 2-dimensional analysis of Section 3.1. The errors shown for the temperature are the 90 percent errors. For the temperature profiles, data from all 3 instruments were used. The solid lines in the temperature plots represent the universal temperature profiles of Loken et al. (2002), and the dotted horizontal lines mark the confidence limits of the over-all cluster temperature from Table. 2.

2-dimensional analysis results in a larger value for the r_c , as expected due to the coupling between the β -index and the r_c . However, this fit does not represent the data well, especially in the inner cluster regions. The low β values (with the accordingly low r_c) can be understood if one takes into account the fact that the cluster is extended, and the *XMM-Newton* data map only its inner regions. Its surface brightness distribution does not reach the background lev-

els at $r = 10$ arcmin, which is the size of the fitting image region, and there are some difficulties in reliably subtracting the background, as discussed in section 2.2 above. To test for possible effects due to residual background, we performed a 2-dimensional analysis similar to that described above, but with a model comprised of a constant plus a β -model. The inclusion of the constant in the model resulted in best-fitting values for the β -index and the r_c closer to

their ‘canonical’ values, and to the ones found by earlier investigations. We found β -index and r_c values of $0.56^{+0.47}_{-0.17}$ and $193.4^{+101.8}_{-1.9}$ arcsec= $289.9^{+152.6}_{-2.8}$ kpc respectively.

As explained in Section 2.2, we found that the blank-sky background files for the PN instrument require large scaling factors to match the background levels of the Abell 2255 observations, and we therefore decided not to use these blank-sky background files for spectral analysis. For the spatial analysis, the background-subtracted images of Section 3 (which made use of the blank-sky background files) were fitted by a 2-dimensional model. Due to the uncertainties in the scaling factor of the PN camera, we checked the analysis, fitting only the images from the two MOS cameras. We found best fitting parameters consistent with those derived from the full three datasets, as presented above.

We co-added the best fitting model images for the MOS instruments, and a contour plot is overlaid onto the optical image of the cluster in Fig. 2, where we also show the positive (white contours) and negative (black contours) residuals of the fit. As is seen in this image, the cluster centre found by the best-fitting model does not coincide with any of the large galaxies in the field. Additionally, there are positive residuals to the East and West of the X-ray centre that seem to coincide with some galaxies, while the centre of the distribution coincides with a depression in the light distribution.

3.2 Sectors

In order to visualize better the residuals of the 2-dimensional analysis and compare them with the temperature distribution around the cluster centre, we present next the radial profiles along the sectors shown in Fig. 1(a). We obtained the radial surface brightness profiles in the four sectors around the centre α_{cen} , δ_{cen} found in Section 3.1. Each sector was 90 degrees wide and the orientation of all four is shown in Fig. 1(a). A comparison of the radial profiles in each sector with the best-fitting model for each one found by the 2-dimensional analysis in Section 3.1 is presented in Fig. 3. For the surface brightness plot, only data from the MOS1 camera are shown, although all three cameras were used for the analysis. Figure 3 also presents the temperature profiles along the same sectors. Their derivation will be presented in a later section.

4 SPECTRAL ANALYSIS

For the following spectral analysis, we used the clean and filtered event lists produced in Section 2.1. Responses and auxiliary files were generated with RMFGEN-1.48.5 and ARFGEN-1.54.7 respectively. Generally, we model in XSPEC the (0.3-8.0) keV energy range by absorbed thermal models.

4.1 Over-all temperature

Source spectra were extracted in a circular region centred at α_{cen} , δ_{cen} (see Section 3.1), and extending out to 6 arcmin. The background was taken from an annular region adjacent to the source region, between 6 and 10 arcmin from the cluster centre. Spectra from the three XMM-Newton instruments and the two observations were fitted simultaneously

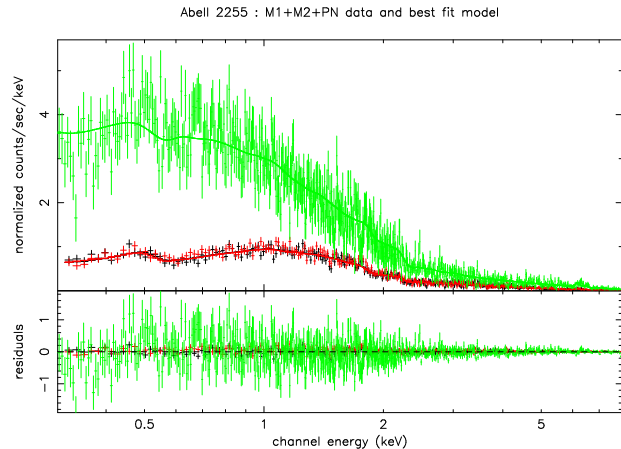


Figure 4. XMM-Newton spectra of the inner 6 arcmin of Abell 2255. The data from the two MOS cameras are shown as black and grey crosses, and give the same count rate. The spectra accumulated from the PN instrument are always the ones at higher cnt s⁻¹ keV⁻¹. For clarity, data from observation 0112260801 are only shown. The best-fitting model, and the residuals of the fit are also included.

Table 2. Spectral properties

Parameter	Value
kT (keV)	6.90 ± 0.29
N_H ($\times 10^{20}$ cm ²)	1.43 ± 0.29
Z (Z_\odot)	0.24 ± 0.05
L_x^1 ($\times 10^{44}$ erg s ⁻¹)	2.780 ± 0.042
$\chi^2/\text{d.o.f.}$	2554/2372
R_{200} (Mpc/arcmin)	2.11/23.5
M_{500} ($\times 10^{14}$ M_\odot)	4.44
β_{spec}	1.305

NOTES: ¹: (0.3-8.0) keV, unabsorbed X-ray luminosity

by a *mekal* model modified by the absorbing column (N_H). During the fitting procedure, the N_H , the temperature of the plasma (kT), the metallicity (Z), and the normalization were left free to vary.

The XMM-Newton spectra, the best-fitting model, and the residuals of the fit are shown in Fig. 4.1. For clarity, data only from the observation 0112260801 are included, but the spectra accumulated from the other observation are very similar. The results of this fitting procedure are shown in Table 2. In the same table we also list the overdensity radius R_{200} and the mass M_{500} , derived from the cluster temperature, using the relation of Evrard, Metzger, Navarro (1996). In the same table we also list the value of $\beta_{\text{spec}} = (\mu m_p \sigma^2)/(k_B T_{\text{ICM}})$, where μ , σ are the mean molecular weight ($\mu = 0.6$), and velocity dispersion of the cluster ($\sigma = 1200$ km s⁻¹ – see in the introduction).

The derived cluster temperature and abundances are generally in good agreement with the results from the *Einstein* (David et al. 1993; White, Jones, & Forman 1997),

and *ASCA* (White 2000) satellites. A significant discrepancy arises when comparing with the *ROSAT* results of Burns et al. (1995), and Feretti et al. (1997). This issue will be investigated and discussed later in this paper (Section 5).

4.2 Temperature distribution

As mentioned in the introduction, Davis & White (1998) showed that the temperature distribution in Abell 2255 might be more complex than can be described with just a single global temperature. Feretti et al. (1997) also noted a difference in the hardness ratio data between the eastern and western regions of the cluster. As will be clear from the next sections, the *XMM-Newton* data also argue for the existence of such an asymmetry.

4.2.1 Sectors

In order to disclose the azimuthal variations of the temperature profiles, we obtained spectra in concentric annuli in the four sectors shown in Fig. 1(a). The width of each annulus was 1 arcmin, yielding spectra with adequate number of counts for the full spectral modelling. We performed exactly the same fitting procedures as in Section 4.2.1. The derived temperature profiles are shown in Fig. 3 along with the corresponding surface brightness distributions, whose derivation was discussed earlier in this paper.

Recently, Loken et al. (2002) derived a ‘universal temperature profile’ for clusters using numerically simulated clusters. To derive the profile, they used only simulated clusters that appeared relaxed, discarding the ones that showed signs of recent disturbances due to mergers. They found that the temperature declines with the distance (r) from the cluster centre as $1.33T_0(1 + 1.5r/\alpha_x)^{-\delta}$ keV, where T_0 is the ‘global’ temperature, and $\alpha_x = r_{\text{vir}}$ the virial radius of the cluster. Fits to their simulated data led to a value for the exponent of δ of 1.6, and the normalization of 1.33. This theoretical temperature profile shows the expected behaviour of a relaxed cluster at a temperature T_0 . Deviations from it should be signs that the cluster is not relaxed. This theoretical profile is in good agreement with much observed data [see, for example Sakelliou & Ponman (2004), and references therein]. However, Loken et al. (2002) found that they could not reproduce the central core seen in the observational temperature profiles of De Grandi & Molendi (2002), and that the model over-predicts the temperature in the central regions (for $r < 0.1r_{\text{vir}}$). A disagreement between the *XMM-Newton* data of Abell 2255 and the ‘universal temperature profile’ might also be seen in Fig. 3 in the inner $r < 2$ arcmin. However, it has been found that the ‘universal temperature profile’ of Loken et al. (2002) is in good agreement with the observational temperature profiles at large radii. Support for this belief comes from the recent temperature profiles obtained from *Chandra* (Vikhlinin et al. 2005) and *XMM-Newton* data (Piffaretti et al. 2005), that follow very closely the theoretical profile, and argue for a temperature decline at large radii. In the temperature plots of Fig. 3 we show with solid lines the temperature profile for Abell 2255, as predicted by the above equation of Loken et al. (2002). As r_{vir} we used the $R_{200}=2.11$ Mpc, and the ‘global’ temperature is $T_0=6.90$ keV given in Table 2. We have to note

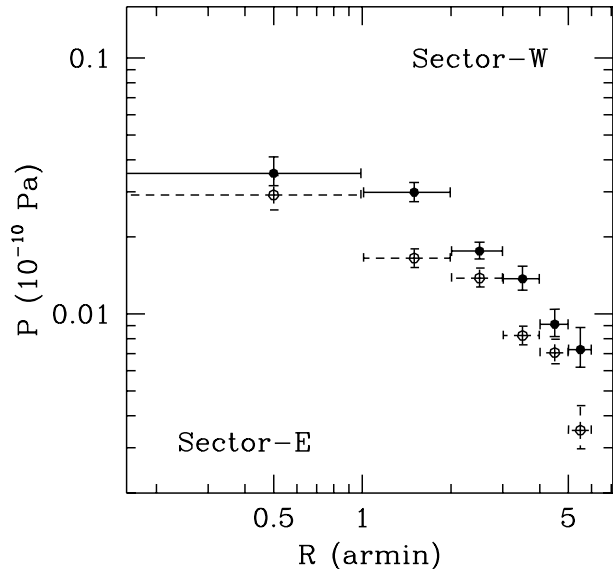


Figure 5. Comparison of the pressure profiles along the sectors -W (filled symbols) and -E (open symbols).

though, that the profiles of Fig. 3 do not extend out to large radii, but are restricted to $r < 0.25R_{200}$. A small temperature decline at $0.25R_{200}$ is expected by the theoretical profile as can be seen in Fig. 3.

A few striking properties for the temperature structure of Abell 2255 emerge from the inspection of these figures: i) the low temperature in the inner 2 arcmin in sector-E, and ii) the high temperature in the outer (3-6) arcmin region in sector-W. Along sector-N and sector-S, the temperature profiles appear the most regular of the four, showing the gas to be nearly isothermal at the global temperature, and consistent with the theoretical universal temperature profile.

The above spectral fits resulted in a normalization ($norm$) for the *mekal* component in each spatial bin. Assuming that the hot X-ray emitting component at the derived temperature is distributed uniformly in the entire volume of each spherical bin, and using the dependency of $norm$ on the density (n) ($norm \propto \int n^2 dV$) we derived a density for the plasma in each bin. With the densities and temperatures of each bin in each sector we calculated the pressure profiles shown in Fig. 5 where we compare the pressures along sector-E and sector-W. The pressures for the other two sectors (sector-N and -S) are always between the ones along sector-E and -W. This comparison provides further evidence that the main disturbances occur along the East-West direction of the cluster.

4.2.2 Temperature map

The analysis of the previous sections revealed an asymmetry in the temperature distribution between the eastern and western regions of the cluster. In order to visualize better these anomalies and understand their 2-dimensional extent we constructed the temperature map shown in Fig. 4.2.2 by accumulating source counts in square regions around the

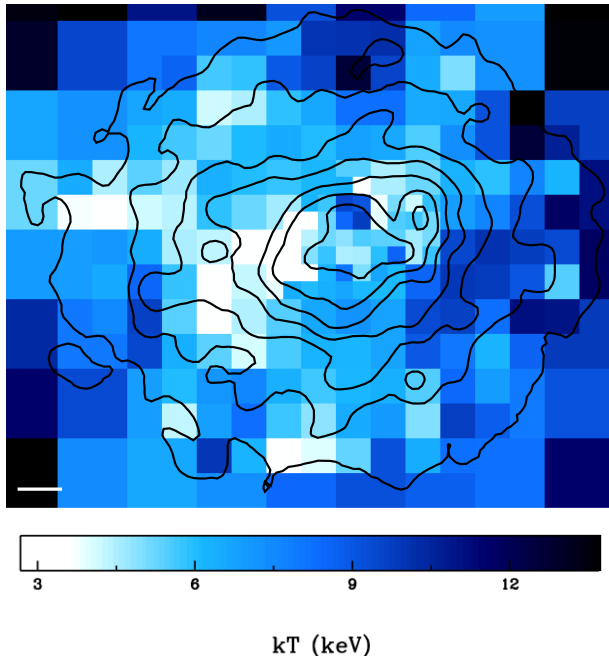


Figure 6. The temperature map of the central region of Abell 2255 overlaid by the X-ray contours shown in Fig. 1(b). The horizontal bar is 1 arcmin in length.

cluster centre. The initial region was 25×25 arcmin wide. This region was subdivided into 2×2 bins. Subsequently, each bin was divided again into smaller bins, until the number of counts in each bin dropped below a minimum number of counts of $n_{\min} = 2000$, which is the minimum number of counts we require in each bin, in order to obtain accurate temperature values. Any bins containing $< n_{\min}$ adopted the properties of the corresponding larger bin. For the creation of the temperature map we used only the longest of the two *XMM-Newton* observations (obs=0112260801). As the background we used the blank-sky background files, and the scaling factors we found in Section 2.2. The spectral fits for each bin were performed again in *XSPEC*, with the N_{H} being fixed to the best-fitting value found in Section 4.1. The metal abundances were left free to vary.

To guide the eye in Fig. 4.2.2 we overlay the resultant temperature map with contours of the X-ray emission shown in Fig. 1(a) and (b). This image shows clearly the temperature distribution within the core of Abell 2255, and supports the findings of Section 4.2.2. In particular it shows that: i) the cool emission to the East of the cluster centre is spread over a wide region, mainly along sector-E, ii) galaxy A [see Fig. 1(b)] is not associated with any cold emission as will be discussed in Section 5, but instead there is cold emission to the north-east of it, and iii) the regions to the south and south-west of galaxy A are hotter, reaching in some places temperatures of the order of $\sim(9-10)$ keV. This emission does not appear associated with galaxy B, which is not listed as an active galaxy. Additionally, Fig. 1(b) shows clearly that galaxy B does not contribute to the X-ray emission.

5 DISCREPANCY BETWEEN *XMM-Newton* AND *ROSAT* TEMPERATURES

As noted in Section 4.1, a significant discrepancy arises when comparing the temperatures derived from *XMM-Newton* and *ROSAT*: with the *XMM-Newton* data we find a global temperature of ~ 6.9 keV; the spectral fits to the *ROSAT* All Sky Survey (RASS) data resulted in a much lower temperature of $1.9^{+2.3}_{-0.4}$ keV (Burns et al. 1995) for the central parts of Abell 2255. Feretti et al. (1997), using pointing *ROSAT* observations, derived a similarly low temperature of 3.5 ± 1.5 keV. The temperature map of Davis & White (1998) supports the above *ROSAT* findings, since they found a temperature of $3.5^{+3.7}_{-1.4}$ keV for the inner 1.5 arcmin region. However, it has to be noted, that none of these investigations argue for the presence of a traditional ‘cooling flow’ in the cluster. Its absence is also supported by the lack of a strongly centrally peaked surface brightness distribution (see, for example, the surface brightness plots of Fig. 3).

The reason for the above discrepancy might be simply that the source regions used for the *ROSAT* analysis were not centred on the cluster centre as defined here, but more towards the galaxies A and B [see Fig. 1(b)], which might host cooler X-ray atmospheres. The recent investigation of the X-ray properties of the cluster galaxies with *Chandra* did not include galaxy A and B (Davis et al 2003), because unfortunately they lie on a CCD gap. As is apparent from Fig. 1(b) and 2, significant emission from galaxy A was registered by *XMM-Newton*. Attempts to fit the *XMM-Newton* spectra from small regions around galaxy A did not result to any temperatures lower than ~ 5.6 keV. To obtain the temperature around galaxy A, we accumulated counts in a circular region centered on the galaxy with a 0.5 arcmin radius. We fitted the (0.3-5.0) keV spectrum with an absorbed *mekal* model. The N_{H} and Z were fixed to the values shown in Table 2. The fitting procedure resulted to a best-fitting temperature of $7.25^{+2.95}_{-1.69}$ keV ($\chi^2/d.o.f.=85/93$). The temperature map of Fig. 4.2.2 also supports these findings.

The lack of centrally concentrated cold gas is also apparent from the analysis of the Sections 4.2.2 and 4.2. In those Sections we found evidence for lower temperatures in the cluster (towards its eastern regions), but again not as low as required to support the *ROSAT* results.

On the other hand, the discrepancy might be due to an inherent artefact of the modelling of the *ROSAT* data. The fits of a two (or more) thermal components by a single one in the *ROSAT* narrow energy band might have unavoidably resulted to a single cluster temperature that is lower than it should. As we found in the previous sections the inner regions of Abell 2255 are dominated by two temperatures of ~ 5.5 and ~ 7 keV. Recently, Mazzotta et al. (2004) investigated the effect of a single temperature model fits to a two temperature plasma when observed with *Chandra* or *XMM-Newton*. They found that in some cases the single temperature fits might be ‘acceptable’ (regarding the reduced χ^2 of the fit), leading to a temperature that does not correspond to any real temperature in the cluster.

In order to investigate the above possibility as the explanation for the discrepancy between *ROSAT* and *XMM-Newton* we simulated in *XSPEC* *ROSAT* PSPC spectra comprised of two thermal models: one at a temperature of 5.5 keV and the second at 7 keV. The metallicity of both was

equal to the metallicity we derived in Section 4.1 ($Z=0.24$), and both models were absorbed by the Galactic column. We also assumed an equal contribution by both to the composite thermal model, choosing equal normalizations of the two models, that additionally yielded a luminosity equal to the L_x of Table 2. The choice for equal contributions from the two temperatures is justified by the fact that the normalizations we find from the spectral fits shown in Fig. 3 for the low and high temperatures are very similar. The exposure time of the simulated spectrum was set to that of the ROSAT PSPC observation (~ 15 ksec).

We modelled in XSPEC the (0.1-2.4) keV simulated spectrum by a single *Raymond-Smith* model, using the ROSAT response `pspc_gain1_34.rsp`. The fitting procedure found a temperature of $7.6^{+3.6}_{-1.8}$ keV and reasonable values for the N_H and Z . However, the quality of the fit was poor, resulting to a $\chi^2_\nu \sim 0.5$. This result indicates that the reason for the low ROSAT temperatures is not due to the incorrect modelling of the ROSAT spectrum. We have to note though, that the ROSAT PSPC spectrum, the quality and residuals of the fit that resulted to the previously quoted low temperatures have not been presented, making a further comparison with our results difficult. As mentioned before, the XMM-Newton temperatures are consistent with the ones found by *Einstein* and *ASCA*. Unfortunately, the disagreement with the ROSAT results still remains, but further investigations are outside the scope of this paper.

6 SUMMARY AND DISCUSSION

The XMM-Newton data and analysis, presented in the previous sections show strong evidence that Abell 2255 is far from our idealized picture of a ‘relaxed’ cluster. It has suffered a merger event in its recent past, and the signatures of such a turmoil are still visible: the X-ray emission is elongated along the East-West direction, aligned with a chain of galaxies; the temperature distribution does not follow the universal temperature profile of Loken et al. (2002); the X-ray emission is not centered at any galaxy. Especially, the temperature structure shows the kind of disturbances expected during/after a merger event. Although we derive a ‘global’ temperature for the cluster of ~ 6.9 keV, it is not isothermal at this temperature. Its eastern regions are cooler at $\sim (5-6)$ keV, and towards the West the temperature reaches ~ 8.5 keV. Following the temperature asymmetry, there is a pressure imbalance between East and West (see Fig. 5), which is mainly driven by the temperature inequality.

Over the last years, thanks to the XMM-Newton and *Chandra* we have witnessed the complicated structure of the ICM in merging/evolving clusters. Additionally, numerical simulations of merging clusters have advanced to such an extent that can show us the details of the evolution of a merger event. The challenge now is to match the observations with the simulations and understand how the final cluster is formed.

For unequal mass mergers, simulations show (e.g., Takizawa 1999, Roettiger et al. 1997) that after the cores of the two subclusters collide, the smaller and cooler cluster continues travelling away from the collision location, leaving a cool trail along its trajectory. Two shocks are generated during the collision, that travel along the collision axis towards

opposite directions. One ‘front’ shock is leading the smaller subcluster, and it is diffuse. The ‘back’ one is more compact, and propagates towards the opposite direction. The X-ray properties of Abell 2255 support the idea that it is a merger remnant after the core collision phase. Specifically, there is a correspondence with the results, for example, presented by Takizawa (1999). A comparison of Fig. 4.2.2 with the temperature structure in the merger remnant of his fig. 8 at $t = 4.75$ Gyr shows a striking similarity. This correspondence can be also found with other numerical work.

The comparison of the temperature distributions along sector-E and -W of Fig. 3 shows that there is a temperature increase from the cluster average (~ 6.9 keV) up to ~ 8.5 keV. A possible explanation for this is that it is due to a shock wave. If this is the case, using eqn. (2) from Markevitch, Sarazin & Vikhlinin (1999), we find that the Mach number of the relative motion is $M \sim 1.24$, which implies a velocity of $\simeq 2400$ km s $^{-1}$ (the sound speed in Abell 2255 is $c_s = 1940$ km s $^{-1}$), and a compression factor of $1/x \sim 1.36$. For the above calculation we used $\gamma = 5/3$, a preshock temperature of $kT_0 \sim 6.9$ keV, and postshock temperature of $kT_1 \sim 8.5$ keV. If this is the ‘back’ shock seen in the simulations, and it has been travelling at $v = 2400$ km s $^{-1}$, and if the core crossing happened where the current cluster centre is, we find that the cores collided some $t = s/v \sim (4 \text{ arcmin})/(2400 \text{ km/s}^{-1}) \sim 0.15$ Gyr ago. Such a shock wave would have increased the flux by an amount of $\Sigma_1/\Sigma_0 = 1.36^2 \sim 1.85$. If we compare the flux at a distance of ~ 5 arcmin from the cluster centre in Sector-W with the flux along sector-S and -N, we find that the measured Σ_1/Σ_0 is not more than ~ 2 . Of course, the details of the structure depends on the initial conditions and projection effects.

Being guided again by the numerical work [e.g., Takizawa (1999), Randall, Sarazin, Ricker (2002)] we note that the collision of the subclusters’ cores during the ‘core-crossing’ phase results in a sharp and brief increase of the luminosity and temperature. Afterwards, the cluster expands adiabatically, resulting in a decrease of its temperature and luminosity. The luminosity drops below its initial value, which is defined as the sum of the initial luminosities of the two subunits. The temperature on the other hand, remains at the same levels as the initial temperature (before the collision) until a later stage of the merging process, at which it increases more mildly, due to the collapse and accumulation of the cluster material towards the new cluster centre. Thus, if a cluster is at a stage after the dramatic ‘core-crossing’ phase, its luminosity should be high, but not as high as during the violent sub-clusters collision, and lower than the initial total luminosity of the system.

In order to locate Abell 2255 on the L-T relation, we compare its properties with the L-T relation derived by Markevitch (1998). We calculated the cluster bolometric luminosity, and extrapolated it out to $1h^{-1}$ Mpc, in the same manner as in Markevitch (1998). Although Abell 2255 does not host a traditional ‘cooling flow’, we exclude the inner regions of the cluster to be consistent with the analysis of Markevitch (1998). The derived luminosity, $L_{\text{bol}} \simeq 12.13 \times 10^{44}$ erg s $^{-1}$, is almost double the expected L_{bol} of a ~ 7 keV cluster, according to the L-T relation, if we compare with fig. 2 in Markevitch (1998). During the next stages of the merging process, the luminosity of the remnant will re-

main almost unaltered, while its temperature will increase as explained earlier. This temperature increase may be such that its temperature and luminosity come into agreement with the L-T relation, and will stay at that condition until the final merger remnant is formed. Being guided again by the the numerical simulations we find that Abell 2255 will settle down to a single remnant in some $\sim(2-3)$ Gyr.

ACKNOWLEDGMENTS

The Digitized Sky Survey (DSS), and the NASA/IPAC Extragalactic Database (NED) have been used. The present work is based on observations obtained with *XMM-Newton*, an ESA science mission with instruments and contributions directly funded by ESA Member States and the USA (NASA). IS acknowledges the support of the European Community under a Marie Curie Intra-European Fellowship.

REFERENCES

- Buote D.A., 2001, ApJ, 553, L15
 Burns J.O., Roettinger K., Ledlow M., Klypin A., 1994, ApJL, 427, L87
 Burns J.O., Roettinger K., Pinkney J., Perley R.A., Owen F.N., Voges W., 1995, ApJ, 446, 583
 David L.P., Slyz A., Jones C., Forman W., Vrtilek S.D., Arnaud K.A., 1993, ApJ, 412, 479
 Davis D.S., White III R.E., 1998, ApJ, 492, 57
 Davis D.S., Miller N.A., Mushotzky R.F., 2003, ApJ, 597, 202
 De Grandi S., Modendi S., 2002 ApJ, 567, 163
 Evrard A.E., Metzler C.A., Navarro J.F., 1996, ApJ, 469, 494
 Feretti L., Böhringer H., Giovannini G., Neumann D., 1997, A&A, 317, 432
 Giovannini G., Feretti L., 2000, New Astronomy, 5, 335
 Giovannini G., Tordi M., Feretti L., 1999, New Astronomy, 4, 141
 Govoni F., Murgia M., Feretti L., Giovannini G., Dallacasa D., Taylor G.B., 2005, A&A, 430, L5
 Loken C., Norman M.L., Nelson E., Burns J.O., Bryan G.L., Motl P., 2002, ApJ, 579, 571
 Lumb D. 2002, 'EPIC BACKGROUND FILES, XMM-SOC-CAL-TN-0016, issue 2.0
 Markevitch M., 1998, ApJ, 504, 27
 Markevitch M., Sarazin C.L., Vikhlinin A., 1999, ApJ, 521, 526
 Mazzotta P., Rasia E., Moscardini L., Tormen G., 2004, MNRAS, 354, 10
 Mullis C.R., Henry J.P., Gioia I.M., Böhringer H., Briel U.G., Voges W., Huchra J.P., 2001, ApJL, 553, L115
 Piffaretti R., Jetzer Ph., Kaastra J.S., Tamura T., 2005, A&A, 433, 101
 Pratt G.W., Arnaud M., 2002, A&A, 394, 375
 Randall S.W., Sarazin C., Ricker P.M., 2002, ApJ, 577, 579
 Roettiger K., Loken C., Burns J.O., 1997, ApJS, 109, 307
 Sakelliou I., Ponman T.J., 2004, MNRAS, 351, 1439
 Takizawa M., 1999, ApJ, 520, 514
 Vikhlinin A., Markevitch M., Murray S.S., Jones C., Forman W., Van Speybroeck L., 2005, astro-ph/0412306
 White D.A., 2000, MNRAS, 312, 663
 White D.A., Jones C., Forman W., 1997, MNRAS, 292, 419
 Yuan Q., Zhou X., Jiang Z., 2003, ApJS, 149, 53